

Deep-learning-based acceleration of MRI for radiotherapy planning of pediatric patients with brain tumors

Shahinur Alam^{1,*}, Jinsoo Uh^{3,*}, Alexander Dresner⁴, Chia-ho Hua³, and Khaled Khairy^{1,2,*}

¹Center for Bioimage Informatics, St. Jude Children's Research Hospital, Memphis, TN 38105, USA

²Department of Developmental Neurobiology, St. Jude Children's Research Hospital, Memphis, TN 38105, USA

³Department of Radiation Oncology, St. Jude Children's Research Hospital, Memphis, TN 38105, USA

⁴Philips Healthcare, Gainesville, FL, USA

Correspondence*:

Shahinur Alam

Center for Bioimage Informatics, 262 Danny Thomas Place, St. Jude Children's Research Hospital, Memphis, TN 38105, USA
shahinur.alam@stjude.org

Khaled Khairy

Center for Bioimage Informatics, 262 Danny Thomas Place, St. Jude Children's Research Hospital, Memphis, TN 38105, USA, khaled.khairy@stjude.org

2 ABSTRACT

3 Magnetic Resonance Imaging (MRI) is a pivotal non-invasive diagnostic and radiotherapy
4 planning tool, offering detailed insights into the anatomy and pathological conditions of the
5 human body, and in monitoring neurological, musculoskeletal, and oncological diseases. The
6 relatively extensive scan time compared to other medical imaging modalities is stressful for
7 patients, who must remain motionless in a prolonged imaging procedure that prioritizes reduction
8 of imaging artifacts and an increase in data quality. This is particularly challenging for pediatric
9 patients who require extra measures for managing voluntary motions such as anesthesia. Several
10 computational approaches attempt to reduce the scan time (namely, fast MRI), which record
11 fewer measurements and then digitally recover full information from this limited set in a post-
12 acquisition reconstruction step. However, most fast MRI approaches have been developed with
13 diagnostic MRI in mind, without addressing reconstruction challenges specific to scanning for
14 radiation therapy (RT) planning. In this work, we developed a deep learning-based method called
15 DeepMRIRec for MRI reconstruction from highly undersampled raw data acquired with RT-specific
16 receiver coils. We evaluated our method against fully sampled k-space data of T1-weighted MR
17 images acquired from 73 pediatric brains with tumors/surgical beds using loop and posterior
18 coils (12 channels). We compared DeepMRIRec to several state-of-the-art deep learning-based

19 reconstruction methods using our dataset with and without applying virtual compression of coil
20 elements. DeepMRIRec reduced image acquisition time by a factor of four producing a structural
21 similarity (SSIM) score of 0.96 ± 0.006 , surpassing state-of-the-art methods and demonstrating
22 its suitability for highly accelerated MRI scanning for pediatric RT planning.

23 **Keywords:** MRI, radiotherapy, deep learning, image reconstruction, data augmentation, parallel imaging

1 INTRODUCTION

24 Magnetic Resonance Imaging (MRI) is an essential imaging modality in treatment planning for radiotherapy
25 (RT) because of its superior soft tissue contrast defining target volumes and other anatomical structures.
26 The absence of imaging-related ionizing radiation exposure in MRI is particularly beneficial for pediatric
27 patients. However, one of the downsides of MRI is the relatively long scan time. This poses significant
28 challenges in managing patient movement, impacts patient comfort and overall throughput. Younger
29 patients may require anesthesia during the scan (typically patients under 8 years of age). Long scan
30 times necessitate high anesthesia dosages, which raises the potential risk of neurocognitive consequences
31 associated with accumulated anesthesia (Banerjee et al., 2019).

32 In conventional MRI, scan time is proportional to the number of phase encoding steps/lines captured in
33 k-space. Accelerated MRI scanning (also known as fast MRI) can be achieved either by increasing the
34 sampling rate or undersampling raw data in k-space, both of which produce unwanted artifacts. Examples
35 of MRI sequences that increase sampling rate include turbo spin/gradient echo sequences and echo-planar
36 imaging which require hardware enabling the desired strengths of radiofrequency/gradient pulses (Bernstein
37 et al., 2004). Conventional undersampling methods include partial Fourier techniques (McGibney et al.,
38 1993) and parallel imaging (Griswold et al., 2002; Pruessmann et al., 1999; Lustig et al., 2007; Lustig and
39 Pauly, 2010), which utilize the conjugate symmetry in k-space and the spatial dependency of channel-wise
40 data from individual coil elements, respectively, to reconstruct images containing sub-Nyquist artifacts
41 (e.g., aliasing or Gibbs ringing). Such conventional fast MRI methods can be further advanced by low-rank
42 modeling (Halдар, 2013) or compressed sensing (Lustig et al., 2007; Jaspán et al., 2015), which utilizes
43 the sparsity of MR images in the transformed domain. However, sparse transformations are often limited
44 in encoding complex image features, and the computational complexity results in lengthy reconstruction
45 time. The major challenges of conventional MRI reconstruction methods are (Lebel, 2020):- 1) they force
46 clinicians to sacrifice either image quality or spatial resolution, 2) reconstruction time is not well suited for
47 clinical settings that demand low latency, 3) poor subsampling of k-space produces more artifacts, and 4) it
48 is expensive as the number of coils increases. Hence, fast MRI acquisition and reconstruction are still an
49 active research topic.

50 Recent advancement in Artificial Intelligence (AI) brought a breakthrough in object detection (Ahmed
51 et al., 2018; Alam et al., 2020a; Alam, 2021; Alam et al., 2015, 2020b), behavioral and facial expression
52 recognition (Anam et al., 2014), and super-resolution (Dong et al., 2014; Ledig et al., 2017) among
53 others. Deep learning methodology, a branch of AI/ML (LeCun et al., 2015), and publicly available MRI
54 datasets such as fastMRI(Zbontar et al., 2018) shifted the paradigm for MRI data reconstruction marking
55 substantial progress in mitigating the temporal constraints of MRI scans. The latency of MRI reconstruction
56 from undersampled k-space data is now shorter than ever with emerging deep learning based methods
57 (Hammernik et al., 2018; Zhu et al., 2018; Hyun et al., 2018; Wu et al., 2023; Liu et al., 2021; Malkiel
58 et al., 2019; Souza et al., 2019; Lebel, 2020). These computational models have been instrumental in
59 fast imaging, reconstruction, and post-processing tasks, enabling the reduction of scan times with only

60 small compromise in image quality. Various studies corroborate the effectiveness of these techniques in
61 surpassing conventional approaches, showcasing the versatility and adaptability of machine learning and
62 deep learning in optimizing acquisition strategies (Lebel, 2020).

63 Numerous machine learning and deep learning frameworks, such as Convolutional Neural Networks
64 (CNN) and Recurrent Neural Networks (RNN), have been explored for their effectiveness in accelerating
65 MRI scans. For example, Hammernik et al. (2018) developed a variational network for MRI reconstruction
66 that preserves the natural appearance of MR images as well as pathologies; Zhu and colleagues (Zhu
67 et al., 2018) presented a data driven approach called AUTOMAP (automated transform by manifold
68 approximation) for mapping MRI sensor data to the image domain; Hyun and co-workers (Hyun et al.,
69 2018) developed a U-net (Ronneberger et al., 2015) based model to reconstruct images from single channel
70 MRI; Wu et al. (2023) used the Swin Transformer (Liu et al., 2021) and combined k-space consistency to
71 improve MRI reconstructions; Lebel (2020) developed a deep CNN based pipeline called *AIRTM* Recon
72 DL to remove truncation artifacts and increase sharpness in MRI images; Desai et al. (2023) proposed a
73 self-supervised learning consistency training methods for MRI reconstructions.

74 However, the Deep learning-based fast MRI methods mentioned above have been developed with
75 diagnostic images in mind and do not account for the unique challenges in MRI for RT planning. Unlike
76 diagnostic imaging, RT-specific MRI on MR-RT simulators or MR-integrated linear accelerators often
77 utilize receiver coil configurations with smaller numbers of coil elements and/or additional gaps from the
78 body to accommodate immobilization devices or to minimize interference with radiation beams (Paulson
79 et al., 2015; Raaymakers et al., 2017; Hua et al., 2018). This may result in compromised signal intensities
80 in the channel-wise images (see Figure 1). Consequently, previously developed fast MRI methods may
81 not be readily applicable as they are based on parallel MRI reconstructions utilizing redundancy across
82 channel-wise images. Moreover, MRI reconstructions produced by conventional and emerging methods
83 may not always be well suited for mission critical applications that require rich spatial information. Our
84 goal, ultimately, is to develop automated tools that are sensitive enough for delineating tumors and for
85 understanding biological processes such as the progression of pediatric cancers. This necessitates diagnostic
86 images showing internal structures at high contrast; with easily discernible boundaries, and preservation of
87 high frequency information while maintaining the lowest possible scan time. In addition, we need to ensure
88 that radiation oncologists are not misled by a very plausible –but incorrect– reconstruction. Towards that
89 end, we evaluated previously developed deep learning-based methods and propose an improved method
90 that accounts for the RT coil configuration. We focused on cranial imaging in this study as the majority of
91 our treatment cases involve brain tumors and brain images. Among the multitude of previous methods,
92 we selected Hammernik et al. (2021) as our benchmark because it facilitates evaluation of multiple deep
93 network models with various regularization networks and data consistency layers.

2 DATASET AND METHODS

94 2.1 Dataset Details

95 This study uses k-space raw data of T1-weighted MR images from 73 pediatric and young adult patients
96 (aged 1-23 years) who were treated for common pediatric brain tumors at St. Jude Children’s Research
97 Hospital. The MR images were acquired on a 1.5T scanner (Ingenia, Philips Healthcare, Gainesville, FL,
98 USA) for the purpose of planning radiation treatment. These scans utilized a receiver coil configuration
99 accommodating immobilization devices such as a head mask and cushion, and which comprised flexible
100 bilateral loop coils and the posterior coil embedded in the patient table. This coil configuration provided a

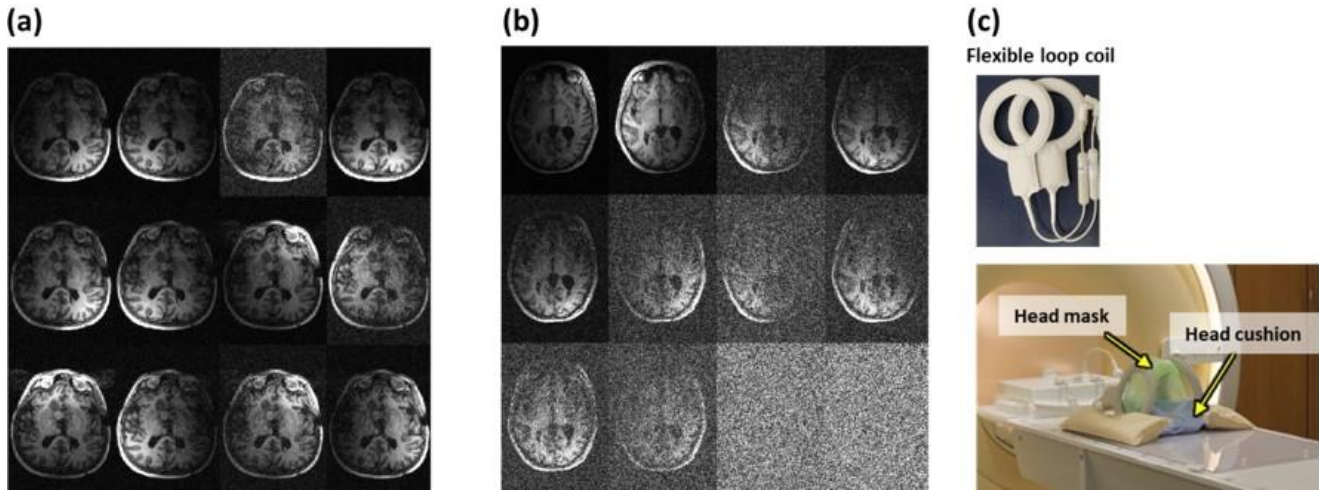


Figure 1. Comparison of channel-wise images from individual coil elements acquired by (a) a diagnostic 15 channel receiver coil versus (b) a loop coil-based configuration for RT imaging. (c) The loop coil-based coil configuration for cranial imaging is illustrated. In addition to the loop coils, coils embedded in the patient table are automatically engaged. Image intensities are often noisy and nonuniform across channels

101 total of 14 channels for the MR signals. We included the data from 12 channels; excluding 2 channels that
 102 gave weak signals and were inconsistently used. The MR images were acquired by a three dimensional
 103 turbo field echo sequence with the inversion recovery pre-pulse, where the frequency encoding was applied
 104 to anterior-posterior directions and phase encoding was applied to the other two directions. The repetition
 105 time (TR), echo time (TE), and inversion time (TI) were 2100ms, 3.5ms, and 1050ms, respectively. The
 106 scan time was typically 6 min and 25 s. To accommodate the two dimensional deep network, we mapped
 107 the original three dimensional data to two dimensions by performing a Fourier transform in the longitudinal
 108 dimension, and cropping out the superior or inferior slices of the brain. In addition, matrices of all images
 109 were adjusted to the same size of 256×192 by zero-padding to the periphery of k-space when smaller. The
 110 resulting field-of-view (FOV) in the left-right and anterior-posterior directions ranged from 159 to 183 mm
 111 and from 220 to 252 mm, respectively; in-plane resolutions were in the range of 0.83 – 0.95 mm and 0.86 –
 112 0.98 mm, respectively. The slice thickness was 2 mm and the number of slices ranged from 56 to 69.

113 2.2 Benchmark method

114 Reconstruction of MRI from undersampled raw data can be formulated (Equation 1) as an inverse problem
 115 (Knoll et al., 2020).

$$\hat{x} = \underset{x}{\operatorname{argmin}} \|Ax - y\|^2 + \lambda R(x) \quad (1)$$

116 Here, x and y correspond to the vectorized image and raw data in k-space, respectively. The forward
 117 encoding operator $A = MFS$, is composed of an undersampling mask (M), Fourier transform (F), and
 118 sensitivity mapping (S). Since estimation of the true image x from the undersampled data is ill-posed,
 119 a regularization term $R(x)$ providing apriori information with proper weighing λ is required to avoid
 120 overfitting. In the evaluated benchmark method, a U-shaped network (UNET) (Ronneberger et al., 2015) and
 121 down-up network (DUNET) (Yu et al., 2019) compose the regularization term. Options for the gradient step
 122 of the data consistency terms included gradient descent (GD), proximal mapping (PM), and variable splitting
 123 (VS), which are detailed in the literature (Hammernik et al., 2021). A four-fold undersampling was simulated

124 by applying a mask, that fully samples 10% of the central k-space and only 16.67% of the remaining 90%
 125 peripheral k-space, on the original fully sampled raw data. MR images reconstructed from the undersampled
 126 raw data are evaluated against images from the fully sampled data. Sensitivity maps are estimated by using
 127 the Berkeley Advanced Reconstruction Toolbox (BART;<https://github.com/mrirecon/bart>)
 128 which implements an eigenvalue method (namely, ESPIRiT) (Uecker et al., 2014) on the 10% fully-sampled
 129 central k-space data. Following the default hyperparameters, we used a learning rate of 0.0001, number
 130 of iterations 16, and initial λ of 10. The network model was trained for 100 epochs with the RMSprop
 131 optimizer.

132 2.3 Summary of the DeepMRIRec workflow

133 The full workflow for MRI reconstructions is shown in Figure 2. In order to train our DeepMRIRec
 134 network, we first developed an undersampling mask (see section Undersampling k-Space) to find an optimal
 135 selection of sampling points and used this to undersample the full k-space data, simulating a four-fold scan
 136 speedup. Second, we applied the established Generalized Autocalibrating Partially Parallel Acquisitions
 137 (GRAPPA)[1] method to estimate missing values and reduce artifacts. Then, the GRAPPA-reconstructed
 138 k-space information was converted into image space using an Inverse Fourier Transformation (IFT). Finally,
 139 we developed a UNET-based model, which we trained on these GRAPPA-reconstructed images as an
 140 enhancer model to improve on the GRAPPA result. During inference, reconstruction of MRI images
 141 acquired at four-fold speed is performed following steps 3 to 6 in Figure 2. Comparison with the benchmark
 142 method is formulated as follows:

$$\hat{x} = UNET(\operatorname{argmin} \|Ax - y\|^2 + \lambda \|(G - I)Fx\|^2) \quad (2)$$

143 The term in outer parenthesis indicates the GRAPPA-reconstructed image which satisfies data consistency
 144 (the first term) with the acquired data and calibration consistency (the second term) wherein the GRAPPA
 145 matrix G constrains the linear relationship between neighboring k-space points. A key difference from the
 146 benchmark method is that the deep network (UNET) encompasses the data consistency term as well, rather
 147 than composing only the regularization term. Subsequently, the input images to the network can be easily
 148 augmented by using conventional image transformations. By contrast, an augmentation of the k-space data
 149 would be required for the benchmark method, which is not readily feasible.

150 2.4 Undersampling K-Space

151 The primary goal of undersampling/subsampling is acceleration of image acquisition without loss of data
 152 quality. The byproduct of undersampling is an increase in aliasing and random image noise. Finding an
 153 efficient and optimal undersampling technique that reduces the aliasing effect received significant attentions
 154 in the recent literature (Razumov et al., 2023; Gaur and Grissom, 2015; Terpstra et al., 2020; Zhou et al.,
 155 2022). Although the majority of MRI is performed by acquiring k-space along a Cartesian trajectory,
 156 non-Cartesian (Wright et al., 2014) methods are also used (Zbontar et al., 2018; d’Arcy et al., 2002; Zhou
 157 et al., 2022). Non-Cartesian sampling has several benefits over Cartesian: 1) it is less sensitive to motion,
 158 2) it produces better image contrast, and 3) it allows ultra-short echo times, among others. Unfortunately, it
 159 is more challenging to reconstruct images from non-Cartesian sampled k-space, and harder to implement
 160 in clinical settings. On the other hand, Cartesian sampling methods are straightforward and amenable to
 161 fast inverse Fourier transformation to reconstruct images from k-space. We explored various Cartesian
 162 undersampling methods (Zbontar et al., 2018) and proposed a new one that works best for both our dataset,
 163 as well as publicly available fastMRI data (Zbontar et al., 2018). We developed a mask (Figure 3) to

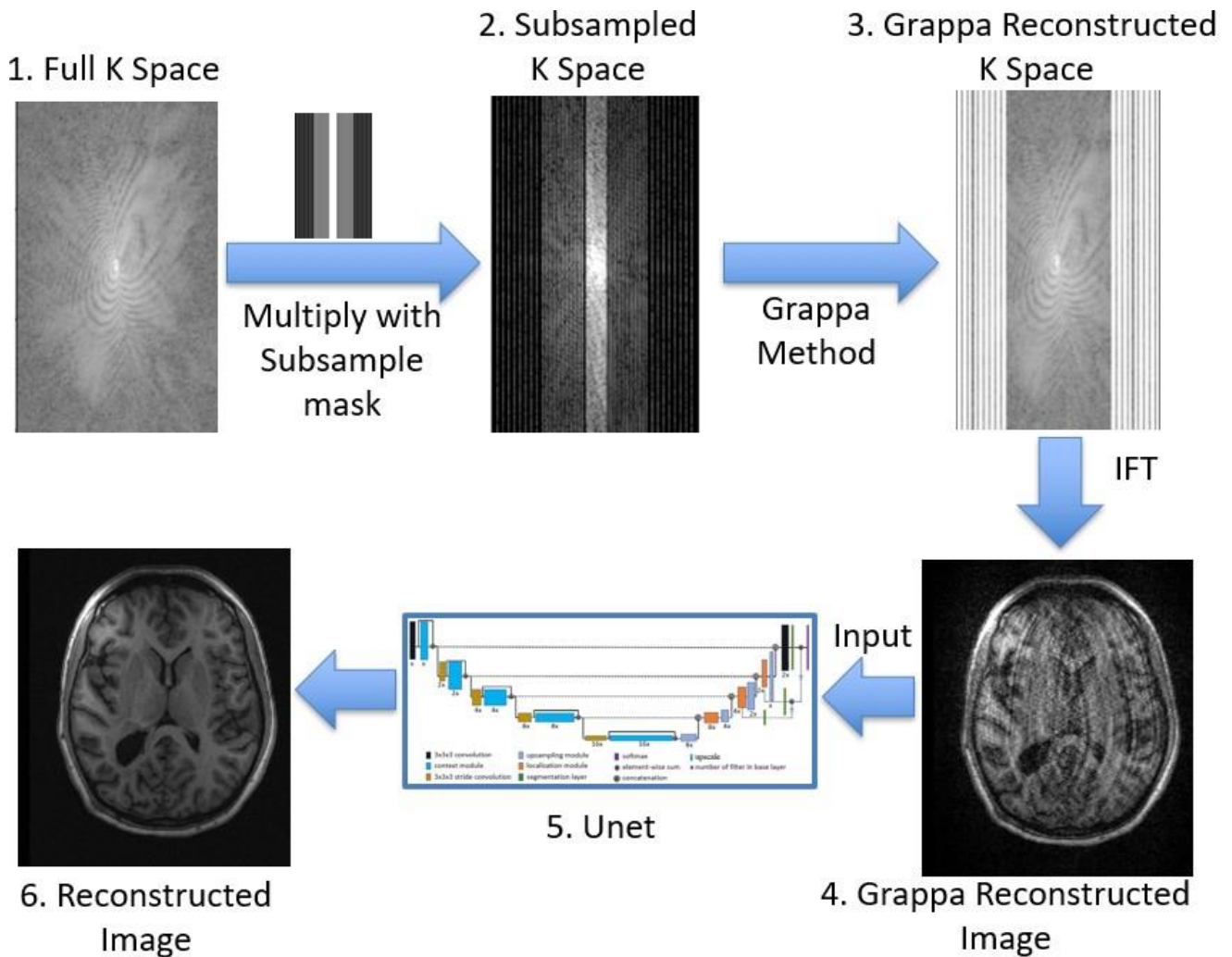


Figure 2. DeepMRIRec workflow: steps 1-6 for training and steps 3-6 for inference

164 retrospectively undersample full k-space data by a factor of 4. Our strategy is to give a higher sampling rate
 165 in the central k-space lines, despite the potential risk of compromising high-frequency information, to fully
 166 leverage the image information enriched towards the central k-space. The proposed 4-fold undersampling
 167 includes the fully sampled 10% central k-space as in the conventional scheme. However, the random
 168 sampling rates in the 90% peripheral regions was not spatially uniform. More specifically, the unilateral
 169 45% peripheral region was divided into equally spaced 4 sections, and an 8:4:2:1 ratio of sampling rates
 170 were assigned from the proximal to distal sections (See Figure 3, four sections on each side of central
 171 k-space are separated by red dotted lines). The resultant acquisitions in these sections comprised 4%, 2%,
 172 1%, and 0.5% of the entire k-space, making the sum of bilateral peripheral acquisitions 15% [i.e., $(4 + 2 +$
 173 $1 + 0.5) \times 2 = 15$]. We added a random offset to pick k-space lines from left and right of the center, so that
 174 each data point carries distinctive information. The detailed algorithm and implementation are provided at
 175 <https://github.com/stjude/DeepMRIRec>.

176 2.5 Data Augmentation

177 Data augmentation is a technique to increase the diversity of a training dataset by applying realistic
 178 transformations. This technique reduces model overfitting (Shorten and Khoshgoftaar, 2019) and increases

179 robustness against changes in tissue geometry, contrast, tissue density, field of view, orientation, and
 180 imaging conditions (Halevy et al., 2009; Sun et al., 2017).

181 We thoroughly evaluated various transformation models, image filters and associated parameters to
 182 generate 19 augmented images from each pair (reference and input). The reference images, Y_{RSS} were
 183 obtained by applying Root Sum Square (RSS) on all coil-images obtained from full k-space (see Equation
 184 3, K = full k-space, IFT=Inverse Fourier Transformation. The input undersampled images (I) were obtained
 185 using Equation 4, where M is the undersampling mask and G is the GRAPPA operation. Table 1 shows the
 186 list of transformation models and parameters used. A sample outcome of data augmentation with an elastic
 187 deformation model is shown in **Figure 4**.

$$Y_{RSS} = \sqrt{IFT(K)} \tag{3}$$

Undersampling Mask

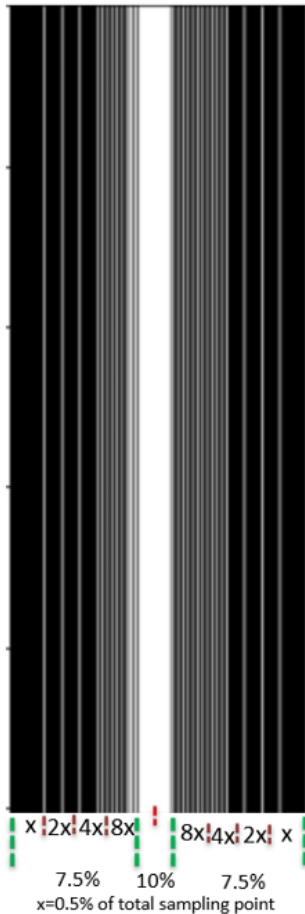


Figure 3. This mask subsamples full k-space by a factor of 4. 10% of the data points are chosen from the central region and 4%, 2%, 1% and 0.5% from peripheral area.

Augmented Image

Original Image

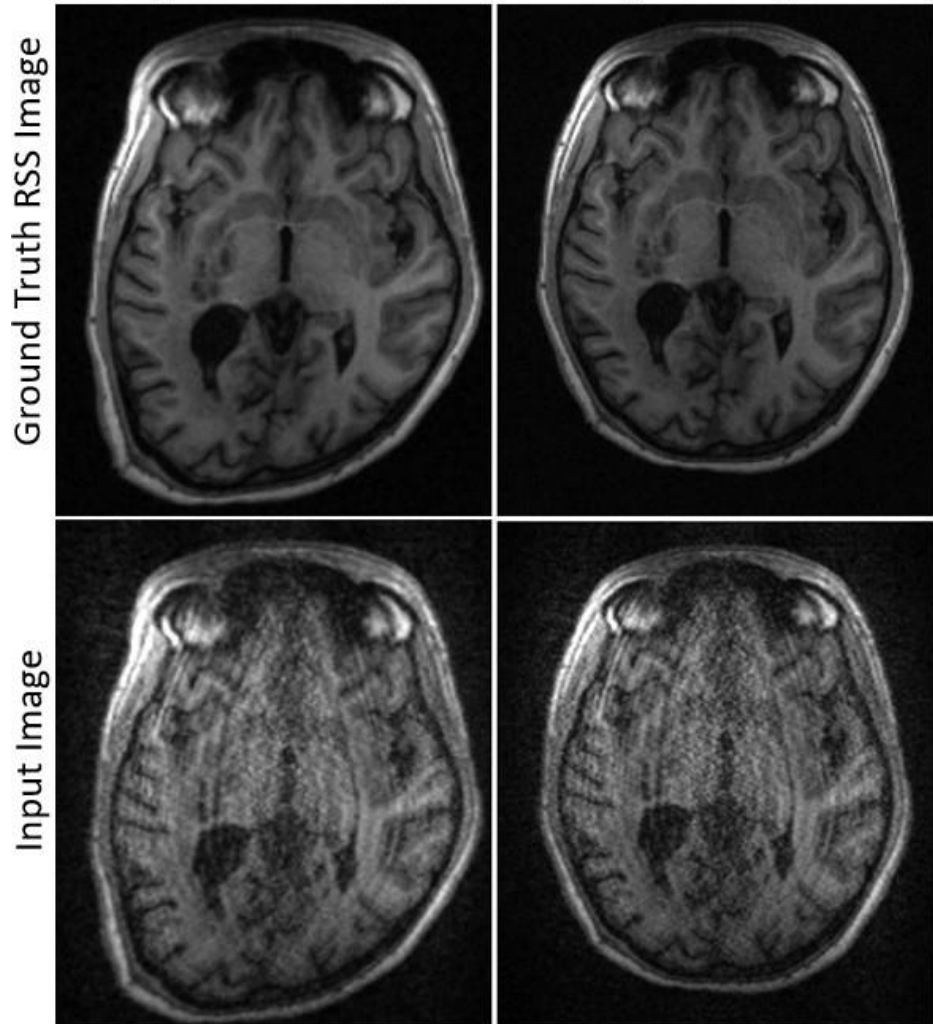


Figure 4. Data augmentation: Left column: augmented images. Right column: original images (input and ground truth pairs). Elastic deformation for a sample image is shown.

$$I = IFT(G(K * M)) \quad (4)$$

Table 1. Methods/Transformation models used for data augmentation. Values of transformation parameters are randomly selected from the range presented within the square brackets.

Method's Name	Parameter Value/Ranges	Augmentation Nature
Horizontal Flip		Produce horizontally flipped images
Dropout	[0.01, 0.05]	Creates images by dropping 1 to 5% voxels
Additive Gaussian Noise	scale [0.0, 12.75]	Creates images by adding noise sampled from Gaussian distributions
GaussianBlur	sigma [0.8, 1.5]	Creates smoothed images
Piecewise Affine	Scale[0.01, 0.07]	Creates images applying an affine transformation to a local grid
Elastic Transformation	alpha ¹ [2.5, 50], sigma ² [1,11]	Creates images by moving voxels locally
Affine Transformation	rotation along Z axis [-20°,20°] scale[0.7 ,1.5] isotropic Translation [-0.01%, 0.01%]	Creates images by applying an affine transformation
Rotation	along Y axis [-30°,30°]	Creates images by rotating around the Y axis

188 2.6 RT-coil Compression

189 DeepMRIRec requires, on average, 120 ms to reconstruct an image from a single RT-coil, including
 190 GRAPPA which requires an average of 115 ms. The reconstruction time of an image by DeepMRIRec
 191 depends on the specific computational resources and the number of channels. Given the highly imbalanced
 192 signal-to-noise ratios across various channels, excluding those with weak signal strength might be beneficial
 193 for reconstruction efficiency, as well as for stabilizing model performance. However, the unique region-
 194 specific information provided by the excluded channels would be lost. Therefore, we investigated the
 195 potential of a virtual coil compression technique proposed by Zhang et al. (2013) to enhance the efficiency
 196 of image reconstruction with preserved or even improved quality of reconstructed images. In this technique,
 197 noisy images are incorporated into high-signal images via an optimized mapping in k-space, thereby the
 198 number of coil elements can be virtually reduced without excluding the region-specific information. In
 199 order to find an optimal number of virtual coils, we compressed the original 12 coil images (Figure 5.a)
 200 into 2, 3, and 4 virtual coil images (Figure 5.b), each of which required a separate training of DeepMRIRec.

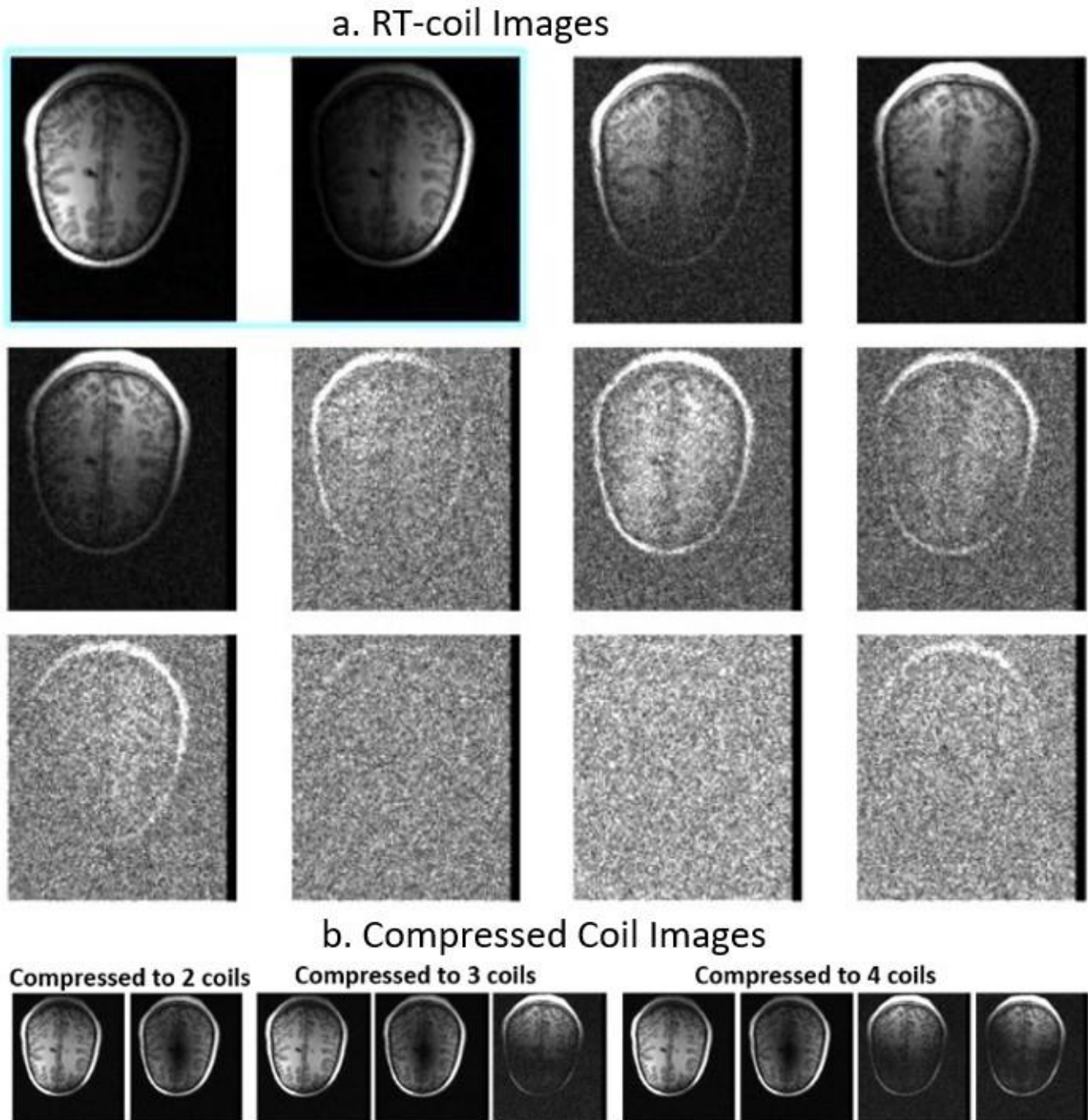


Figure 5. a. RT coil-image for a sample MRI. The signal-to-noise ratio among RT coils are not balanced across MRI volumes; b. Compressed coils

201 2.7 Deep Learning Model

202 2.7.0.1 Network Architecture

203 We designed the DeepMRIRec network architecture (see **Figure 6**) following concepts from the well-
 204 known U-net (Ronneberger et al., 2015), ResNet (He et al., 2016) and DeepBrainIPP (Alam et al.,
 205 2022). DeepMRIRec consists of contracting/encoder (left) and expansive/decoder (right) paths. The

206 contracting path extracts low-level features from input images and compresses/encodes them into high-
 207 level abstractions. The decoder recombines low-level features with higher-level abstractions through skip
 208 connections and performs precise localization. It also has a residual unit (He et al., 2016) to prevent
 209 vanishing gradients which is inherent in very deep networks. On the encoder side, at each layer spatial
 210 resolution is reduced by MaxPooling and the number of filters is increased. On the decoder side, feature
 211 dimension is reduced and higher-level image representations are upsampled to match ground truth images.
 212 The encoder and decoder contain a convolution block in each layer, which is comprised of two two-
 213 dimensional convolution operations (with a 3x3 kernel) followed by BatchNormalization, PreRelu and
 214 Dropout. The BatchNormalization is used to prevent co-variant shift, speed up training, and ease weights
 215 initialization. Unlike contemporary approaches, we considered depth, learning rate, dropout rate, and
 216 number of filters in the base layer as hyperparameters. We used a Bayesian Optimizer (Snoek et al., 2012)
 217 and Keras Tuner (O'Malley et al., 2019) packages to find optimal values of hyperparameters.

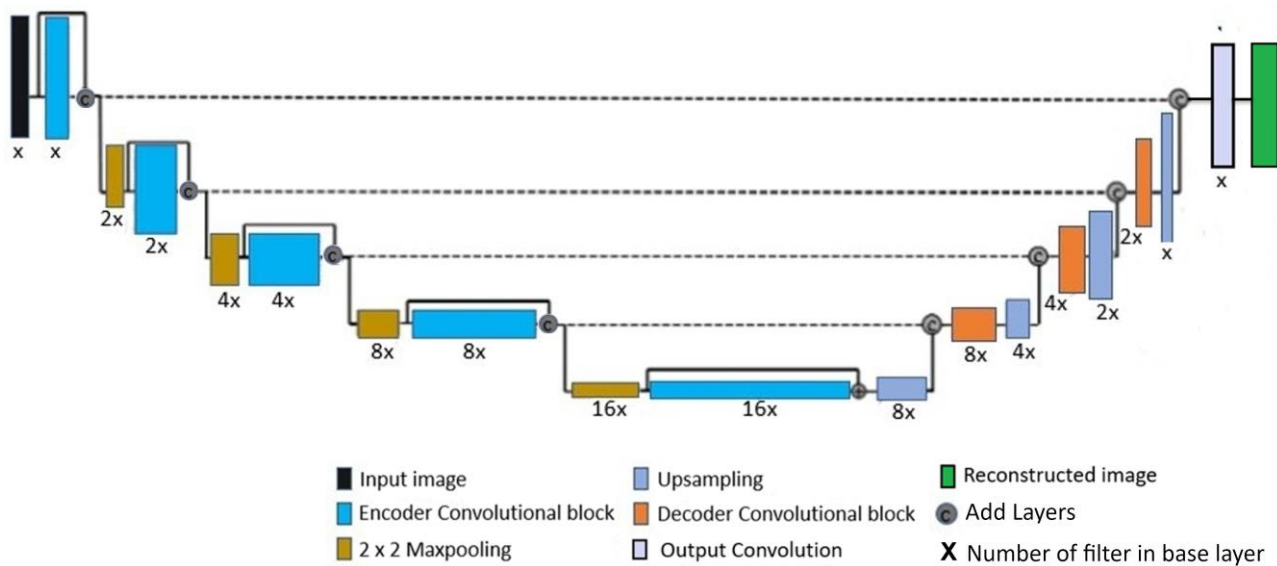


Figure 6. Network Architecture: We designed the DeepMRIRec network architecture by following paradigms from Unet and ResNet. We considered depth and number of filters in the base layer as hyperparameters, which were tuned by Bayesian optimization and grid search.

218 2.7.0.2 Model Training

219 DeepMRIRec was trained on 85348 2D image pairs of dimension 256x192 for 250 epochs, with an early
 220 stopping if the validation loss did not improve, using the Adam optimizer (Kingma and Ba, 2014) on an
 221 NVIDIA A100 80GB GPU system. We used a batch size of 128 and an initial learning rate of 0.0003 with
 222 reduce on Plateau. 80% of the dataset was used for training and the remaining 20% for validation. We
 223 performed channel/coil-wise range normalization of our data. The loss function used to train DeepMRIRec
 224 is shown in equation 5, where $\alpha = 0.0001$, $\beta = 1.0$, and $\gamma = 100$ are regularization parameters obtained
 225 via a grid search. The performance of our model was enhanced by: (1) data augmentation (from 4492 to
 226 85348 2D images), (2) non-uniform undersampling in the peripheral k-space, (3) Bayesian optimization of
 227 hyperparameters, and (4) incorporation of weighted content loss along with L1 and SSIM loss (see loss
 228 function in Equation 5). The conventional loss function such as L1/NMSE is very sensitive to changes

229 in contrast and luminous intensity. Therefore, we added content loss to minimize the effect of changes
 230 in photometric properties. The content loss was obtained from feature maps (F_{GT} , F_S) extracted from
 231 reference and predicted images using a VGG19 (Simonyan and Zisserman, 2014) pretrained model (see
 232 Equations 7 and 8). Figure 7.a shows high level features extracted using VGG19 for various convolutional
 233 layers. The content loss was calculated with layer-wise mean square error (MSE) between feature maps
 234 and weighted based on the depth of the convolutional block (see Equation 6). The optimal weights, (θ_i),
 235 for convolutional blocks ($i=1, 2, 3$ and 4) found from a comprehensive grid search are 0.001, 0.01, 2, and
 236 4 respectively. The optimal values for hyper parameters (learning rate, number of base filters of Unet,
 237 dropout rate, and depth of Unet) were obtained from Bayesian optimizers and determined to be 0.001, 32,
 238 0.05, and 5 respectively.

$$Loss = a * ContentLoss + \beta * L1Loss + \gamma * SSIMLoss \quad (5)$$

239

$$ContentLoss = \sum_{i=1}^4 \theta_i * \frac{(F_{GT}(i) - F_S(i))^2}{L(F_{GT}(i))} \quad (6)$$

240

$$F_{GT} = VGG19(Y_{RSS}) \quad (7)$$

241

$$F_S = VGG19(DeepMRIRec(I)) \quad (8)$$

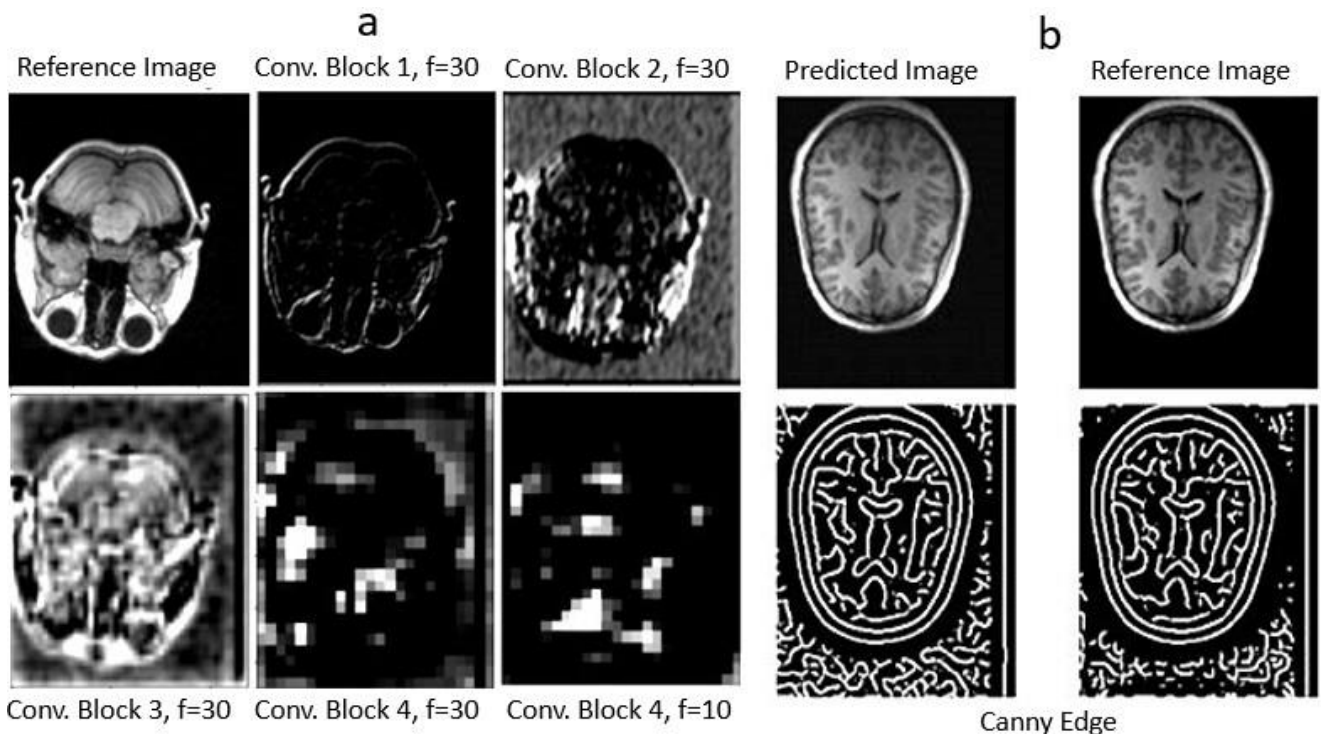


Figure 7. a) Extracted features using VGG19 to calculate content loss. f: index of activation/feature map
 b) high frequency components extracted from predicted and reference images using Canny edge detector to demonstrate how internal structures are aligned.

242 2.7.0.3 Model Evaluation Metrics

243 The proper evaluation metric for MRI reconstruction is still a research question. Global metrics, such
 244 as SSIM, PSNR and NMSE, do not capture the full spectrum of information to assess the quality of
 245 reconstructed images (Nilsson and Akenine-Möller, 2020; Zbontar et al., 2018). PSNR and NMSE are
 246 sensitive to photometric properties such as brightness, contrast, hue and saturation, and do not reflect the
 247 true noise level present in images (Sara et al., 2019). SSIM compares luminance, contrast, and structural
 248 information between two images. However, SSIM has several limitations (Pambrun and Noumeir, 2015):
 249 1) distortions at edges are underestimated, 2) insensitivity to high intensity regions, and 3) instability
 250 in regions with low variance. To address issues of PSNR, NMSE and SSIM, we also included the Dice
 251 Coefficient, and Hausdorff Distance (HD) on high frequency components (HFC) that ensure internal
 252 structures are properly reconstructed. HFC were extracted as a binary map using the Canny Edge Detector
 253 with a sigma of 5. Figure 7. b shows high frequency components extracted from predicted and reference
 254 images. The Dice coefficient is calculated from volumetric similarity using equation 9. To quantify the
 255 difference in edges we measured a Hausdorff Distance using equation 10. R and Y represent pixels in
 256 the binary map extracted from reconstructed and reference (full sampled) images. $d(r,y)$ is the Euclidean
 257 distance between to binary maps.

$$Dice = 2(|R \cap Y|)/(|R| + |Y|) \quad (9)$$

$$Hausdorff = \max(h(R, Y), h(Y, R)) \quad (10)$$

$$h(R, Y) = \max(\min(d(r, y)))$$

3 RESULTS

258 The quantitative evaluation of DeepMRIRec was performed on 20% of our dataset. We present MRI
 259 reconstruction outcomes of our model along with several state-of-the-art deep learning-based models in
 260 Figure 8. Our model reconstruction produces SSIM of 0.96 ± 0.006 , PSNR of 28, and Dice Coefficient,
 261 and HD on HFC are 0.66, and 72 respectively when applied to our dataset. We also trained and validated
 262 our model on a subset of publicly available fastMRI datasets (Zbontar et al., 2018) and it produced a SSIM
 263 of 0.98 whereas the reported best model output to date is 0.96 (Muckley et al., 2021). To test the effect of
 264 data augmentation and content loss we find that both (implemented together) increased our model score
 265 (SSIM) by 4.2%. Figure 9 a-b shows outcomes of our model with and without data augmentation. We
 266 also tested the effect of our proposed undersampling strategy, and find an increase in performance (SSIM)
 267 by 4.0% when compared to conventional methods (see Figure 9 c-d). The coil compression technique
 268 improved our reconstruction score (SSIM) by 1.0% over using the full set of twelve uncompressed coils.
 269 Finally, we investigated reconstruction outcomes when using two, three, and four compressed coils (Table
 270 2). Reconstruction outcomes were found to degrade as we increase the number of virtual coils (data not
 271 shown) because the third, fourth and successive virtual coils contain more noise (see Figure 5.b).

4 DISCUSSION

272 Qualitative evaluation by two radiation oncologists, and the quantitative measures reported above,
 273 demonstrate the utility of DeepMRIRec. As shown in Figure 8, DeepMRIRec produced significantly
 274 better reconstruction outcomes, when compared to other MRI reconstruction models. This is the case

275 when applied to our dataset, as well as when applied to publicly available fastMRI data. The proposed
 276 undersampling strategy (mask), incorporation of GRAPPA to pre-fill the undersampled k-space, data
 277 augmentation, simplified network architecture with Bayesian optimization, and using a customized loss
 278 function to train the model are all factors that collectively permit us to achieve this performance. Although
 279 GRAPPA adds significant computational overhead in our pipeline, it improves performance significantly
 280 (by 9.0%). It is important to keep in mind that the time consumption by GRAPPA increases linearly with
 281 the number of RT-coils. The coil compression technique played a significant practical role in decreasing
 282 the effective number of coils, and consequently saved the time needed to apply GRAPPA. Moreover, this
 283 decreased effective number of coils reduced training and inference times, as well as memory requirements
 284 for computation because the input dimension of the network is smaller (two channels instead of twelve).

285 The results also show that our model, trained on only loop coils, reconstructed images more accurately
 286 than when trained on all coils and that coil-compression not only speeds up MRI reconstructions, but also
 287 recovers the internal details of images more accurately. This is likely due to the noise-suppression and
 288 high frequency component retention inherent in the compression algorithm itself. Without reliance on
 289 coil-compression, network filters could not capture meaningful information in the earlier layers from noisy
 290 images. Instead, the low SNR lead to ambiguities in the higher layers.

291 Finally, our evaluation of selected models, including DeepMRIRec, revealed that they produce
 292 slightly smoothed images when compared to the fully sampled ones. One possible reason is that
 293 the undersampling mask contains more information from the center of the k-space image and picks less
 294 information from peripheral regions, which tend to contain high frequency information. Better future
 295 strategies for undersampling can mitigate this effect and increase reconstruction quality further.

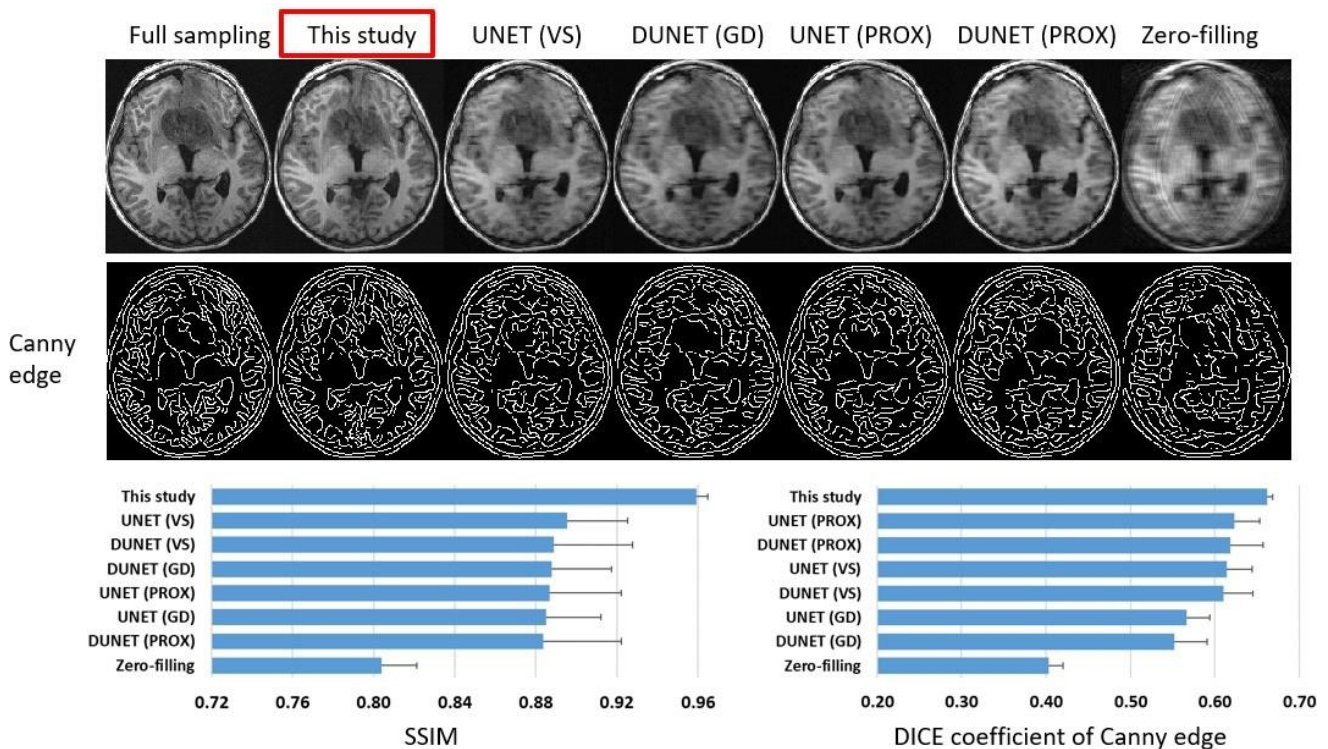


Figure 8. Comparison of reconstructed images using DeepMRIRec versus state-of-the-art methods

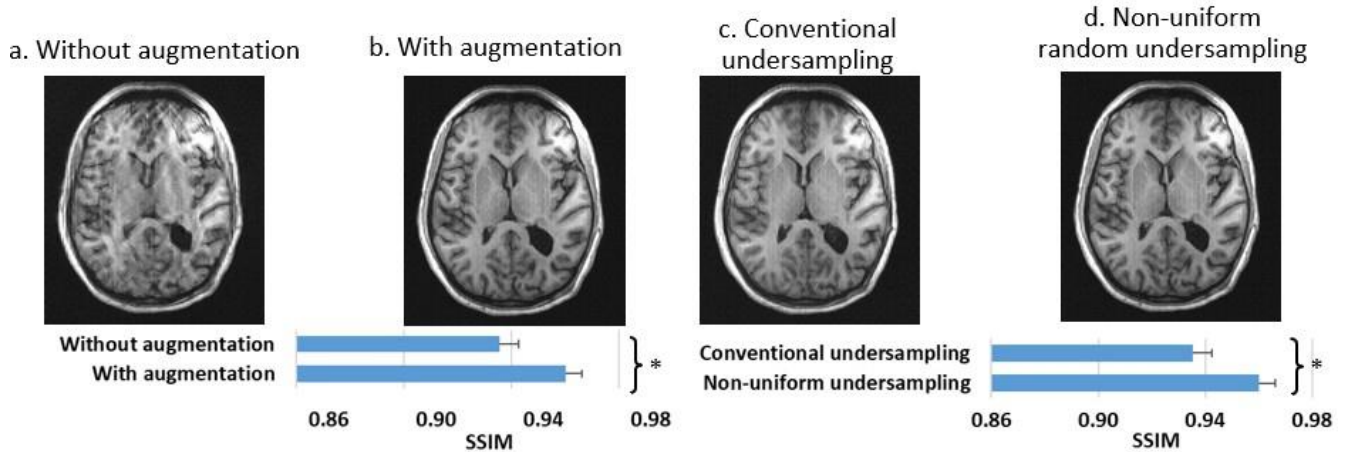


Figure 9. Comparison of reconstructions: a-b) with/without data augmentation c-d) with proposed and conventional undersampling

Table 2. DeepMRIRec: Reconstruction Outcomes

RT-coils	SSIM	PSNR	Dice on HFC	HD on HFC
Compressed coil: 2	0.9646	28	0.66	72
Compressed coil: 3	0.9555	27	0.66	71
Compressed coil: 4	0.9557	26	0.64	70
Loop coil	0.9588	28	0.65	72
12 coils	0.9556	26	0.64	71

5 CONCLUSION

296 In this manuscript, we presented DeepMRIRec for RT-coil specific MRI reconstruction. DeepMRIRec
 297 outperforms state-of-the-art methods, further closing the gap needed to meet demands of mission critical
 298 applications. This study shows that MRI acquisition can be accelerated by four-fold using DeepMRIRec
 299 with minimal compromise in internal details. The method has the potential to reduce the therapeutic burden
 300 carried by patients and to speed up both therapeutic planning and diagnosis.

DATA AVAILABILITY STATEMENT

301 Source code, model weights and sample images are available at [https://github.com/stjude/](https://github.com/stjude/DeepMRIRec)
 302 DeepMRIRec. The dataset will be provided based upon request with institutional approval.

6 ETHICS STATEMENT

303 This study involving human imaging data was approved by St. Jude Institutional Review Board (IRB
 304 Number: 22-1257) and conducted in accordance with the local legislation and institutional requirements.
 305 Written informed consent for participation in this retrospective study was not required from the participants

306 or the minor(s)' legal guardian/next of kin in accordance with the national legislation and institutional
307 requirements.

AUTHOR CONTRIBUTIONS

308 SA: conceptualization, methodology, DeepMRIRec pipeline development, validation, writing original draft
309 and visualization. JU and AD: data collection, data curation, evaluation of contemporary methods, and
310 radiation oncology expert validation. CH: administration, supervision and editing. KK: conceptualization,
311 writing original draft, and supervision. All authors contributed to the article and approved the submitted
312 version.

7 FUNDING

313 This work was supported in part by the American Lebanese Syrian Associated Charities (ALSAC) and the
314 National Cancer Institute (NCI Cancer Support Grants P30CA021765).

ACKNOWLEDGMENTS

315 We wish to thank Mia Panlilio for early discussions in this project.

8 SUPPLEMENTARY MATERIAL

9 CONFLICT OF INTEREST

316 The authors have no conflict of interest to report.

REFERENCES

- 317 Ahmed, F., Mahmud, M. S., Al-Fahad, R., Alam, S., and Yeasin, M. (2018). Image captioning for ambient
318 awareness on a sidewalk. In *2018 1st International Conference on Data Intelligence and Security*
319 *(ICDIS)* (IEEE), 85–91
- 320 Alam, S. (2021). Safeaccess+: An intelligent system to make smart home safer and americans with
321 disability act compliant. *arXiv preprint arXiv:2110.09273*
- 322 Alam, S., Anam, I., and Yeasin, M. (2015). O'map: An assistive solution for identifying and localizing
323 objects in a semi-structured environment. *Journal on Technology and Persons with Disabilities* , 204–231
- 324 Alam, S., Eom, T.-Y., Steinberg, J., Ackerman, D., Schmitt, J. E., Akers, W. J., et al. (2022). An end-to-end
325 pipeline for fully automatic morphological quantification of mouse brain structures from mri imagery.
326 *Frontiers in Bioinformatics* 2, 865443
- 327 Alam, S., Mahmud, M. S., and Yeasin, M. (2020a). An assistive solution to assess incoming threats for
328 homes
- 329 Alam, S., Mahmud, M. S., and Yeasin, M. (2020b). Toward building safer smart homes for the people with
330 disabilities. *arXiv preprint arXiv:2006.05907*
- 331 Anam, A. I., Alam, S., and Yeasin, M. (2014). Expression: A dyadic conversation aid using google glass
332 for people with visual impairments. In *Proceedings of the 2014 acm international joint conference on*
333 *pervasive and ubiquitous computing: Adjunct publication*. 211–214

- 334 Banerjee, P., Rossi, M. G., Angheliescu, D. L., Liu, W., Breazeale, A. M., Reddick, W. E., et al. (2019).
335 Association between anesthesia exposure and neurocognitive and neuroimaging outcomes in long-term
336 survivors of childhood acute lymphoblastic leukemia. *JAMA oncology* 5, 1456–1463
- 337 Bernstein, M. A., King, K. F., and Zhou, X. J. (2004). *Handbook of MRI pulse sequences* (Elsevier)
- 338 d’Arcy, J., Collins, D., Rowland, I., Padhani, A., and Leach, M. (2002). Applications of sliding window
339 reconstruction with cartesian sampling for dynamic contrast enhanced mri. *NMR in Biomedicine: An*
340 *International Journal Devoted to the Development and Application of Magnetic Resonance In Vivo* 15,
341 174–183
- 342 Desai, A. D., Ozturkler, B. M., Sandino, C. M., Boutin, R., Willis, M., Vasanawala, S., et al. (2023).
343 Noise2recon: Enabling snr-robust mri reconstruction with semi-supervised and self-supervised learning.
344 *Magnetic Resonance in Medicine* 90, 2052–2070
- 345 Dong, C., Loy, C. C., He, K., and Tang, X. (2014). Learning a deep convolutional network for image
346 super-resolution. In *Computer Vision–ECCV 2014: 13th European Conference, Zurich, Switzerland,*
347 *September 6–12, 2014, Proceedings, Part IV 13* (Springer), 184–199
- 348 Gaur, P. and Grissom, W. A. (2015). Accelerated mri thermometry by direct estimation of temperature
349 from undersampled k-space data. *Magnetic resonance in medicine* 73, 1914–1925
- 350 Griswold, M. A., Jakob, P. M., Heidemann, R. M., Nittka, M., Jellus, V., Wang, J., et al. (2002). Generalized
351 autocalibrating partially parallel acquisitions (grappa). *Magnetic Resonance in Medicine: An Official*
352 *Journal of the International Society for Magnetic Resonance in Medicine* 47, 1202–1210
- 353 Haldar, J. P. (2013). Low-rank modeling of local k -space neighborhoods (loraks) for constrained mri.
354 *IEEE transactions on medical imaging* 33, 668–681
- 355 Halevy, A., Norvig, P., and Pereira, F. (2009). The unreasonable effectiveness of data. *IEEE Intelligent*
356 *Systems* 24, 8–12
- 357 Hammernik, K., Klatzer, T., Kobler, E., Recht, M. P., Sodickson, D. K., Pock, T., et al. (2018). Learning
358 a variational network for reconstruction of accelerated mri data. *Magnetic resonance in medicine* 79,
359 3055–3071
- 360 Hammernik, K., Schlemper, J., Qin, C., Duan, J., Summers, R. M., and Rueckert, D. (2021). Systematic
361 evaluation of iterative deep neural networks for fast parallel mri reconstruction with sensitivity-weighted
362 coil combination. *Magnetic Resonance in Medicine* 86, 1859–1872
- 363 He, K., Zhang, X., Ren, S., and Sun, J. (2016). Identity mappings in deep residual networks. In *European*
364 *conference on computer vision* (Springer), 630–645
- 365 Hua, C.-h., Uh, J., Krasin, M. J., Lucas Jr, J. T., Tinkle, C. L., Acharya, S., et al. (2018). Clinical
366 implementation of magnetic resonance imaging systems for simulation and planning of pediatric radiation
367 therapy. *Journal of medical imaging and radiation sciences* 49, 153–163
- 368 Hyun, C. M., Kim, H. P., Lee, S. M., Lee, S., and Seo, J. K. (2018). Deep learning for undersampled mri
369 reconstruction. *Physics in Medicine & Biology* 63, 135007
- 370 Jaspán, O. N., Fleysher, R., and Lipton, M. L. (2015). Compressed sensing mri: a review of the clinical
371 literature. *The British journal of radiology* 88, 20150487
- 372 Kingma, D. P. and Ba, J. (2014). Adam: A method for stochastic optimization. *arXiv preprint*
373 *arXiv:1412.6980*
- 374 Knoll, F., Hammernik, K., Zhang, C., Moeller, S., Pock, T., Sodickson, D. K., et al. (2020). Deep-learning
375 methods for parallel magnetic resonance imaging reconstruction: A survey of the current approaches,
376 trends, and issues. *IEEE signal processing magazine* 37, 128–140
- 377 Lebel, R. M. (2020). Performance characterization of a novel deep learning-based mr image reconstruction
378 pipeline. *arXiv preprint arXiv:2008.06559*

- 379 LeCun, Y., Bengio, Y., and Hinton, G. (2015). Deep learning. *nature* 521, 436–444
- 380 Ledig, C., Theis, L., Huszár, F., Caballero, J., Cunningham, A., Acosta, A., et al. (2017). Photo-realistic
381 single image super-resolution using a generative adversarial network. In *Proceedings of the IEEE*
382 *conference on computer vision and pattern recognition*. 4681–4690
- 383 Liu, Z., Lin, Y., Cao, Y., Hu, H., Wei, Y., Zhang, Z., et al. (2021). Swin transformer: Hierarchical
384 vision transformer using shifted windows. In *Proceedings of the IEEE/CVF international conference on*
385 *computer vision*. 10012–10022
- 386 Lustig, M., Donoho, D., and Pauly, J. M. (2007). Sparse mri: The application of compressed sensing for
387 rapid mr imaging. *Magnetic Resonance in Medicine: An Official Journal of the International Society for*
388 *Magnetic Resonance in Medicine* 58, 1182–1195
- 389 Lustig, M. and Pauly, J. M. (2010). Spirit: iterative self-consistent parallel imaging reconstruction from
390 arbitrary k-space. *Magnetic resonance in medicine* 64, 457–471
- 391 Malkiel, I., Ahn, S., Taviani, V., Menini, A., Wolf, L., and Hardy, C. J. (2019). Conditional wgens with
392 adaptive gradient balancing for sparse mri reconstruction. *arXiv preprint arXiv:1905.00985*
- 393 McGibney, G., Smith, M., Nichols, S., and Crawley, A. (1993). Quantitative evaluation of several partial
394 fourier reconstruction algorithms used in mri. *Magnetic resonance in medicine* 30, 51–59
- 395 Muckley, M. J., Riemenschneider, B., Radmanesh, A., Kim, S., Jeong, G., Ko, J., et al. (2021). Results of
396 the 2020 fastmri challenge for machine learning mr image reconstruction. *IEEE transactions on medical*
397 *imaging* 40, 2306–2317
- 398 Nilsson, J. and Akenine-Möller, T. (2020). Understanding ssim. *arXiv preprint arXiv:2006.13846*
- 399 [Dataset] O’Malley, T., Bursztein, E., Long, J., Chollet, F., Jin, H., Invernizzi, L., et al. (2019). Kerastuner.
400 <https://github.com/keras-team/keras-tuner>
- 401 Pambrun, J.-F. and Noumeir, R. (2015). Limitations of the ssim quality metric in the context of diagnostic
402 imaging. In *2015 IEEE international conference on image processing (ICIP) (IEEE)*, 2960–2963
- 403 Paulson, E. S., Erickson, B., Schultz, C., and Allen Li, X. (2015). Comprehensive mri simulation
404 methodology using a dedicated mri scanner in radiation oncology for external beam radiation treatment
405 planning. *Medical physics* 42, 28–39
- 406 Pruessmann, K. P., Weiger, M., Scheidegger, M. B., and Boesiger, P. (1999). Sense: sensitivity encoding for
407 fast mri. *Magnetic Resonance in Medicine: An Official Journal of the International Society for Magnetic*
408 *Resonance in Medicine* 42, 952–962
- 409 Raaymakers, B. W., Jürgenliemk-Schulz, I., Bol, G., Glitzner, M., Kotte, A., Van Asselen, B., et al. (2017).
410 First patients treated with a 1.5 t mri-linac: clinical proof of concept of a high-precision, high-field mri
411 guided radiotherapy treatment. *Physics in Medicine & Biology* 62, L41
- 412 Razumov, A., Rogov, O., and Dylov, D. V. (2023). Optimal mri undersampling patterns for ultimate benefit
413 of medical vision tasks. *Magnetic Resonance Imaging* 103, 37–47
- 414 Ronneberger, O., Fischer, P., and Brox, T. (2015). U-net: Convolutional networks for biomedical
415 image segmentation. In *International Conference on Medical image computing and computer-assisted*
416 *intervention (Springer)*, 234–241
- 417 Sara, U., Akter, M., and Uddin, M. S. (2019). Image quality assessment through fsim, ssim, mse and
418 psnr—a comparative study. *Journal of Computer and Communications* 7, 8–18
- 419 Shorten, C. and Khoshgoftaar, T. M. (2019). A survey on image data augmentation for deep learning.
420 *Journal of Big Data* 6, 1–48
- 421 Simonyan, K. and Zisserman, A. (2014). Very deep convolutional networks for large-scale image
422 recognition. *arXiv preprint arXiv:1409.1556*

- 423 Snoek, J., Larochelle, H., and Adams, R. P. (2012). Practical bayesian optimization of machine learning
424 algorithms. *Advances in neural information processing systems* 25
- 425 Souza, R., Lebel, R. M., and Frayne, R. (2019). A hybrid, dual domain, cascade of convolutional neural
426 networks for magnetic resonance image reconstruction. In *International Conference on Medical Imaging*
427 *with Deep Learning* (PMLR), 437–446
- 428 Sun, C., Shrivastava, A., Singh, S., and Gupta, A. (2017). Revisiting unreasonable effectiveness of data in
429 deep learning era. In *Proceedings of the IEEE international conference on computer vision*. 843–852
- 430 Terpstra, M. L., Maspero, M., d’Agata, F., Stemkens, B., Intven, M. P., Lagendijk, J. J., et al. (2020).
431 Deep learning-based image reconstruction and motion estimation from undersampled radial k-space for
432 real-time mri-guided radiotherapy. *Physics in Medicine & Biology* 65, 155015
- 433 Uecker, M., Lai, P., Murphy, M. J., Virtue, P., Elad, M., Pauly, J. M., et al. (2014). Espirit—an eigenvalue
434 approach to autocalibrating parallel mri: where sense meets grappa. *Magnetic resonance in medicine* 71,
435 990–1001
- 436 Wright, K. L., Hamilton, J. I., Griswold, M. A., Gulani, V., and Seiberlich, N. (2014). Non-cartesian
437 parallel imaging reconstruction. *Journal of Magnetic Resonance Imaging* 40, 1022–1040
- 438 Wu, Z., Liao, W., Yan, C., Zhao, M., Liu, G., Ma, N., et al. (2023). Deep learning based mri reconstruction
439 with transformer. *Computer Methods and Programs in Biomedicine* 233, 107452
- 440 Yu, S., Park, B., and Jeong, J. (2019). Deep iterative down-up cnn for image denoising. In *Proceedings of*
441 *the IEEE/CVF conference on computer vision and pattern recognition workshops*. 0–0
- 442 Zbontar, J., Knoll, F., Sriram, A., Murrell, T., Huang, Z., Muckley, M. J., et al. (2018). fastmri: An open
443 dataset and benchmarks for accelerated mri. *arXiv preprint arXiv:1811.08839*
- 444 Zhang, T., Pauly, J. M., Vasanawala, S. S., and Lustig, M. (2013). Coil compression for accelerated
445 imaging with cartesian sampling. *Magnetic resonance in medicine* 69, 571–582
- 446 Zhou, B., Schlemper, J., Dey, N., Salehi, S. S. M., Sheth, K., Liu, C., et al. (2022). Dual-domain
447 self-supervised learning for accelerated non-cartesian mri reconstruction. *Medical Image Analysis* 81,
448 102538
- 449 Zhu, B., Liu, J. Z., Cauley, S. F., Rosen, B. R., and Rosen, M. S. (2018). Image reconstruction by
450 domain-transform manifold learning. *Nature* 555, 487–492